Bubble Dynamics and Directional Marangoni Flow Induced by Laser Heating of Silicon Nanodisk Arrays

THE JOURNAL OF PHYSICAL CHEMISTRY C
A JOURNAL OF THE AMERICAN CHEMICAL SOCIETY

pubs.acs.org/JPCC
Article

Bubble Dynamics and Directional Marangoni Flow Induced by Laser Heating of Silicon Nanodisk Arrays

Published as part of The Journal of Physical Chemistry C special issue "Photothermal and Non-Fluorescent Imaging in Microscopy and Spectroscopy".

Pantea Dara* and Mikael Käll*

Cite This: J. Phys. Chem. C 2025, 129, 5502−5510

Read Online

ACCESS | Metrics & More | Article Recommendations | Supporting Information

ABSTRACT: Gold nanostructures have been extensively used as photothermal heat sources in a variety of studies due to their chemical inertness, biocompatibility, and advantageous thermoplasmonic properties. However, gold nanostructures are prone to surface melting and thermal deformation, which, in some cases, limit their applicability. In this study, we investigate micrometer-sized amorphous silicon nanodisk arrays as a stable and biocompatible alternative for the particular application of photothermally induced microbubble formation and generation of strong directional Marangoni flows in water. By using time-modulated continuous-wave laser heating, we show that the induced flows can move microparticles tens of micrometers across a substrate surface. The direction of particle movement can be preselected by utilizing asymmetric pairs of nanodisk arrays as heat sources or dynamically controlled by altering the laser spot position relative to a symmetric pair of arrays. We also demonstrate that average bubble size and particle displacement positively correlate and crucially depend on the laser modulation frequency. These results are discussed in terms of the temporal dynamics of bubble growth following nucleation. Our findings highlight the potential of using silicon nanostructures as substrates for generating strong thermocapillary flows on the micrometer scale, with potential applications in chemical mixing, pumping, particle sorting, and mass transport.

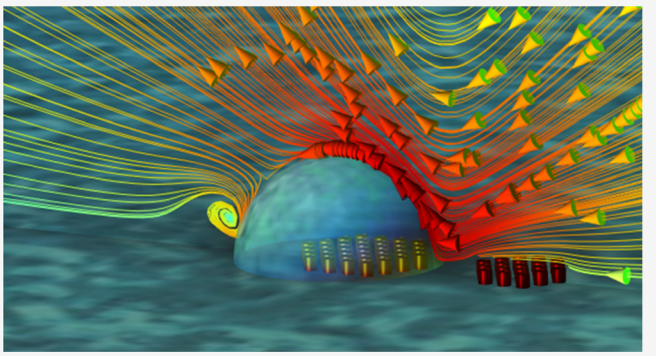

INTRODUCTION

Research and applications of localized optical heat generation based on noble metal nanostructures have surged over the past two decades, giving rise to the flourishing field of "thermoplasmonics".[1] The primary plasmonic material in these studies has been gold, which benefits from being chemically inert and biocompatible while the extreme light localization afforded by plasmon excitation results in a high photothermal conversion efficiency that can be tuned over a wide wavelength range.[2−9] However, gold also faces limitations, in particular surface melting and particle reshaping at elevated temperatures, that may restrict its utility in certain applications.[10,11] One such case is the use of gold nanostructures as a platform for photothermal generation of vapor bubbles,[12−24] where the metal surface temperature needs to reach well above 100 °C to achieve the desired effects.[25]

Over the past several years, nanostructures made from high refractive index dielectrics (HID), in particular silicon, have emerged as a powerful alternative to gold in a wide range of nanophotonics applications.[26−31] In 2017, Zograf et al. demonstrated that Si nanoparticles exhibiting geometric (Mie) optical resonances could serve as effective nanoscale optical heaters, highlighting their higher melting threshold and suitability for Raman nanothermometry.[32] Subsequent studies on HID thermophotonics[33−42] have led to numerous proof-of-principle applications, including sensing and thermometry of protein molecules,[43] controllable drug release in living cells,[44] thermally reconfigurable metaoptics,[45] optical trapping of nanoparticles,[46] and optofluidic transport.[47] To the best of our knowledge, there are so far no reports on photothermal bubble generation based on HID nanostructures. However, already in 1991, Zapka and co-workers showed that pulsed laser heating of Si wafers resulted in the movement and ejection of submicron-sized particles due to explosive boiling of water,[48] a result that led to the introduction of the "steam laser cleaning" technique.[49]

Photothermally induced bubbles generate flow in a liquid through the thermocapillary Marangoni effect, that is, through

Received: November 30, 2024
Revised: February 10, 2025
Accepted: February 21, 2025
Published: March 5, 2025

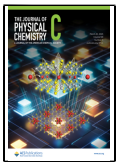

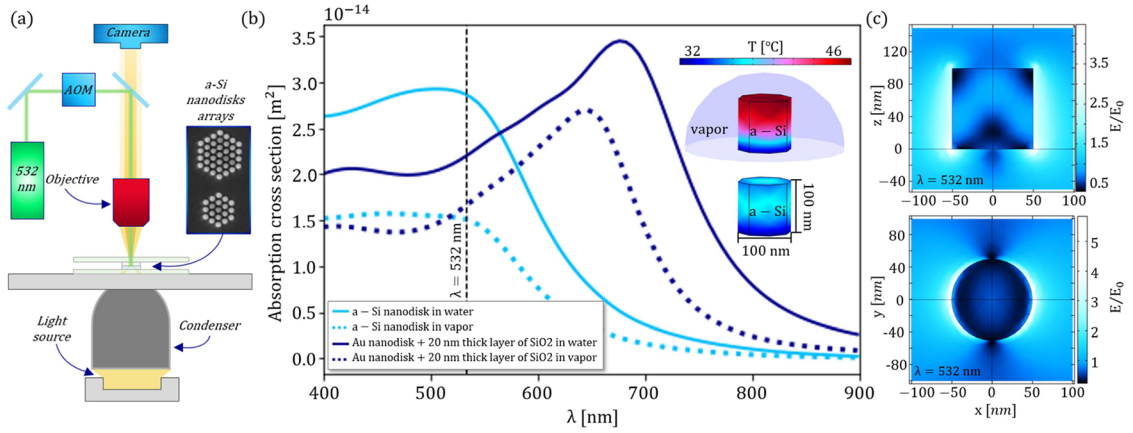

Figure 1. Experimental setup and photothermal properties. (a) Schematic of the experimental setup, which includes a 532 nm wavelength laser source coupled to an acousto-optic modulator (AOM), a camera (Andor Ixon +885 EM-CCD) for tracking bubble dynamics and probe particle movement, and a white light dark-field condenser for illumination of the sample area. The inset shows a scanning electron microscopy image of a typical a-Si nanodisk array sample. (b) Calculated absorption spectra of a single a-Si nanodisk with height and diameter of 100 nm in water and vapor and the corresponding spectra of a single Au nanodisk with height 60 nm, diameter 100 nm, and with a 20 nm protective SiO_2 capping layer. Both structures were optimized for maximum absorption at 532 nm and are situated on a SiO_2 substrate. The inset shows the calculated temperature distribution on the surface of the a-Si nanodisk in water and when covered by a small hemispherical vapor bubble in water, when heated by a plane wave 532 nm laser field with irradiance $I = 0.2$ mW/μm^2. (c) Simulated electric field enhancement factor inside and around an a-Si nanodisk excited at 532 nm in water.

thermal surface tension gradients appearing on the bubble surface due to spatially localized heating. An important theme in recent studies of this effect has been the understanding of the temporal dynamics of bubble growth. It has been established that a bubble typically rapidly grows in size following nucleation, after which it shrinks in a self-oscillatory manner, sometimes involving the exhalation of tiny air bubbles, to a more stable diffusion-limited final growth phase that depends on, for example, water gas content.[20−22,50−55] Equally important from an application point of view is the realization that the Marangoni flow direction can be controlled through in-plane temperature gradients.[56,57]

By applying time-modulated continuous-wave laser heating, Jones et al. demonstrated that the final bubble growth phase could be stabilized by using an isolated micron-sized array of plasmonic gold nanodisks (NDs) as the heating element.[58] This approach results in bubbles that match the size of the array and that can be rapidly modulated in time.[58] Using the same approach, it was later shown that strong transient flows are induced near the plasmonic ND array as microbubbles form and that this transient is followed by a weaker but sustained Marangoni flow.[59] In a subsequent study, we recently showed that the direction of both the transient flow and the ensuing Marangoni flow could be controlled by manipulating the bubble surface tension gradient through the use of pairs of closely spaced gold ND arrays with different sizes or polarization responses.[60]

Inspired by the results summarized above and the growing interest in using HID nanostructures for thermal applications, we report here on the possibility of using amorphous Si (a-Si) ND arrays as a platform for photothermal bubble generation and manipulation of small particles in water. We show that these nanostructures can generate strong directional flows that can be controlled through array asymmetry, illumination position, and modulation frequency, and we establish a correlation between bubble size and flow dynamics. The results demonstrate that Si nanoparticles are a highly competitive alternative to plasmonic particles for studies of photothermal bubbles and induced Marangoni flows and their potential applications in microfluidics.

RESULTS AND DISCUSSION

Methods and Structures. We used hexagonal arrays of cylindrical a-Si NDs, fabricated by electron beam lithography on glass substrates, for photothermal vapor bubble generation. The height of the NDs was set to 100 nm, as given by the available a-Si film thickness, while their radii were optimized to 50 nm through electrodynamic simulations of the optical absorption cross-section at the heating laser wavelength of 532 nm; see the Supporting Information for details. The interparticle edge-to-edge spacing was set to 50 nm and we used close-packed arrays with either 19 or 37 NDs each, corresponding to array widths of 0.7 and 1 μm, respectively. The small diameter of the arrays restricts bubble growth and makes them suitable for use in narrow microfluidic channels.[58] The overall structure design is similar to that previously used for microbubble generation on Au nanodisk arrays.[58−60]

After plasma cleaning to ensure a hydrophilic interface (see Figure S4), the ND arrays were placed in ∼120 μm thin liquid cells filled with air-equilibrated water and illuminated by a 532 nm continuous-wave (cw) Gaussian laser beam with a waist radius $w_0 \approx 11$ μm (fwhm ≈13 μm, Figure S5). Using an acousto-optic modulator (AOM), the laser beam was modulated in a square wave pattern with a frequency $f_m = 1$ Hz−10 kHz and 50% duty cycle. Thus, laser heating is "on" for $1/2f_m$ s and then "off" for the same duration, but the laser intensity and total power are kept constant. This methodology allows us to study the temporal dynamics of bubble formation.[58−60]

To visualize and analyze bubble-induced flows near the substrate interface, we tracked the movement of probe particles (1 or 2 μm diameter polystyrene (PS) beads) and studied the formation and dynamics of single vapor bubbles using white-light dark-field video microscopy. The experimental setup is illustrated in Figure 1a. We also performed fluid dynamics and thermal distribution simulations using the finite element method (FEM) implemented in COMSOL Multiphysics, as detailed in the Supporting Information.

https://doi.org/10.1021/acs.jpcc.4c08101
J. Phys. Chem. C 2025, 129, 5502−5510

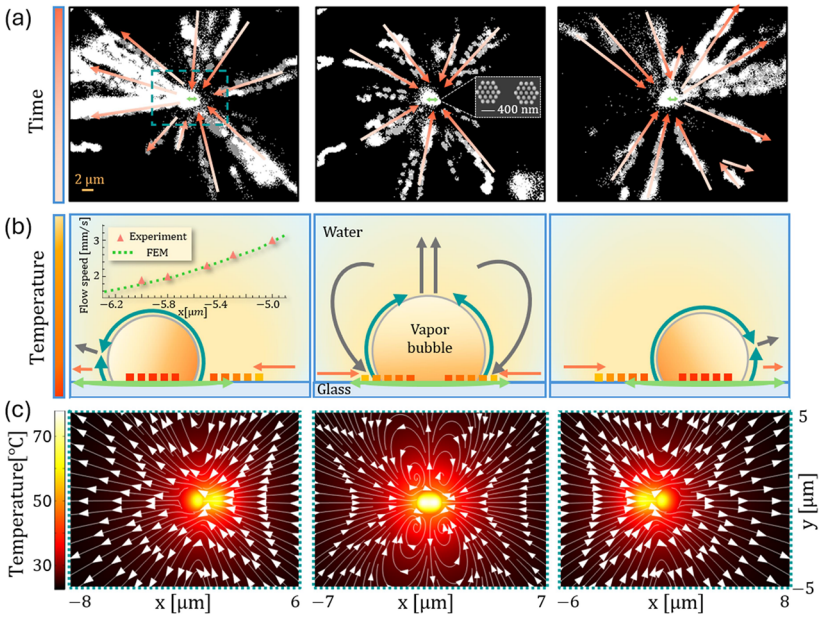

Figure 2. Dynamic control of lateral flow by laser position adjustment. (a) Motion tracks, indicated by graded red arrows, of 1 μm PS beads driven across the substrate surface near a pair of heating arrays, each consisting of 19 a-Si nanodisks, with an edge-to-edge distance of d = 400 nm. A series of images were merged and overlaid to visualize the particle trajectories. The left, right, and center panels show the results of positioning the focal point of the time-modulated Gaussian laser beam ($w_0 \approx 11$ μm, $I_0 = 0.2$ mW/μm^2, $f_m = 100$ Hz) on the left or right array or in between, respectively, as indicated by green points. The inset in the middle panel shows a SEM micrograph of an array pair. (b) Schematic illustration of expected microbubble positions corresponding to the cases in a) and the resulting thermocapillary flow patterns on the bubble surface (dark green arrows), in the bulk (gray arrows), and just above the interface (orange arrows). The expected qualitative variation in local temperature is indicated by the color scale to the left. The inset in the left panel compares the calculated lateral flow speed and the measured speed of PS beads along the symmetry axis connecting the array centers. (c) Simulated lateral flow patterns and the corresponding calculated temperature distribution (color scale) in a plane 0.5 μm above the interface for the illumination cases in (a).

Photothermal Properties. Figure 1b compares the absorption cross-section spectra $\sigma_{abs}(\lambda)$ of the a-Si NDs used here and the Au NDs previously used.[58−60] (height 60 nm, diameter 100 nm, optimized for maximum absorption at 532 nm). The higher absorption of the a-Si NDs in water indicates that these are more effective photothermal heat sources than Au NDs. Moreover, note that the Au ND design includes a 20 nm SiO_2 capping layer. This layer, which is needed to protect the Au structures from thermal reshaping, further reduces the temperature at the water-ND interface.

For an irradiance of 0.2 mW/μm^2 at 532 nm, thermal simulations in a room temperature (T_{RT} = 20 °C) water environment indicate that the average surface temperature T_S of a single a-Si ND reaches ∼38 °C, which corresponds to an excess temperature $\Delta T = T_S - T_{RT}$ that is ∼50% higher than for a single Au ND (inset in Figures 1b and S3). The same calculation for an RT water vapor environment, which has lower thermal conductivity than liquid water, gives $T_S \approx$ 48 and 38 °C for the a-Si and Au NDs, respectively. The advantageous photothermal properties of the a-Si NDs are expected to remain also for the larger arrays used in this study since optical coupling between the nanodisks is very weak. Thus, the total heating power will scale approximately linearly with the number of nanodisks in an array, while the corresponding local temperature increase at a specific point will be approximately given by the sum of the local temperature increases at that point due to each individual particle in an array.[1]

The excellent heating properties of the a-Si ND system partly stem from the magnetic dipole Mie resonance, which is the lowest frequency geometric resonance in HID nanospheres,[32,61] and which dominates the absorption peak near 500 nm seen in Figure 1b (see Figure S1b for a comparison of experimental and calculated scattering spectra). Figure 1c shows the corresponding electric field enhancement distribution at 532 nm, demonstrating a substantial enhancement of the optical field around and within the nanodisk and resulting in σ_{abs} being ∼3.6 times higher than the geometrical cross-section in this particular case.

Directional Flow Control through Varying Illumination Positions. We first investigated to what extent we could control the direction of lateral flow across the glass substrate by varying the focus position of the heating laser spot relative to two identical hexagonal arrays consisting of 19 a-Si NDs each and separated by a d = 400 nm gap (see Figure S6 for the case d = 1.2 μm). We used f_m = 100 Hz and the lowest peak irradiance, I_0 = 0.2 mW/μm^2, which results in bubble nucleation on 19 ND arrays. The induced Marangoni flow close to the substrate surface was visualized by tracking movements of 1 μm diameter PS beads using a camera exposure time of 0.5 ms and a frame rate of 65 Hz.

In Figure 2a (Videos S1−S3), we show overlaid darkfield images of tracer beads for the cases when the laser focal point is positioned on the left or right array or in between the two. Each image sequence is ∼1 s, and the arrows indicate the bead trajectories during this time interval. Clearly, beads are sucked in from the right and ejected to the left if the laser focus is centered on the left array, and vice versa if it is centered on the right, while a focus position between the arrays produces bead movement toward the arrays from all lateral directions. We see no evidence of particle accumulation at the heating structure in the latter case, which implies that beads are ejected vertically out from the observation plane.

https://doi.org/10.1021/acs.jpcc.4c08101
J. Phys. Chem. C 2025, 129, 5502−5510

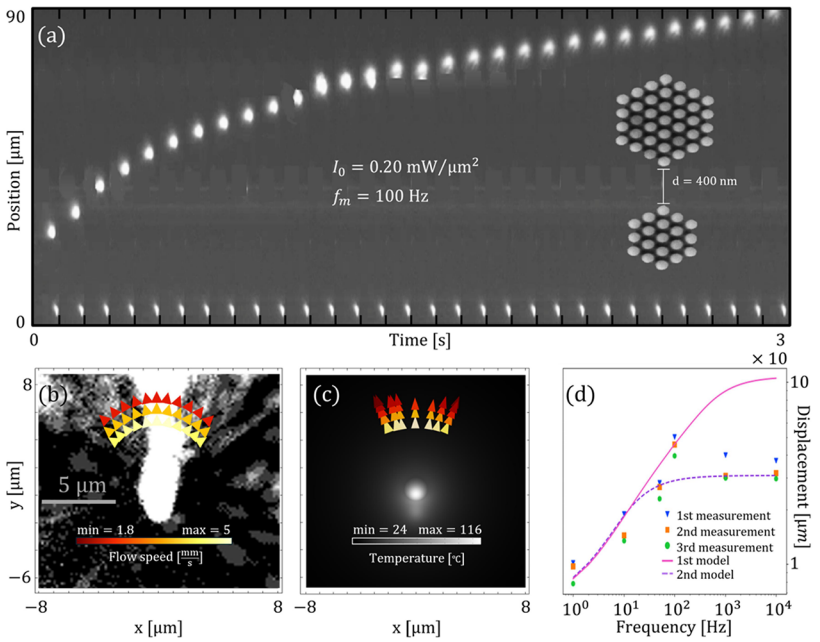

Figure 3. Directional flow and variation in particle displacement with laser modulation frequency for asymmetric a-Si nanodisk arrays. (a) Sequence of video stills showing a 2 μm PS bead as it is pushed away from the arrays by the bubble induced flow. The ND arrays are visible as two adjacent bright white dots at the bottom of the figure. The inset shows a SEM micrograph of the two arrays, containing 37 and 19 NDs, respectively. (b) Overlaid motion tracks of 1 μm PS beads being transported laterally across the substrate due to bubble-induced flow caused by the photothermal heating of an asymmetric pair of a-Si ND arrays. The color scale indicates flow speeds estimated from motion blur. (c) Simulated temperature distribution (gray scale) and lateral flow speeds in a plane 0.5 μm above the interface for the illumination case in (a, b). (d) Probe particle displacement versus modulation frequency f_m on a log−log scale for three asymmetric array pairs. The dashed curve indicates the best fit to the model described in the text obtained by excluding the 100 Hz data, while the full curve shows the best fit obtained by excluding the 1 and 10 kHz data. The heating laser irradiance is I_0 = 0.2 mW/μm^2 in all experiments and the modulation frequency is f_m = 100 Hz in (a) and (b).

The results in Figure 2a are quite remarkable when considering that the total lateral extension of the a-Si ND heating structure (1.8 μm) is much smaller than the laser spot size (fwhm ≈ 13 μm). Since the heating power produced by each array can be approximated as $Q \approx \sigma_{abs} \sum_{i=1}^{19} I(\mathbf{r}_i)$, where $\mathbf{r}_i$ is the position of ND i, we expect that the heat production, at the onset of illumination, should only vary by a few percent between the two arrays as the focal point position varies, but this is apparently enough to change the bubble nucleation site and redirect the flow to the right or to the left or to generate an inward flow pattern.

Figure 2b schematically illustrates our interpretation of these results. When the laser is focused on the center of an array (left and right panels), a bubble nucleates and covers that array. The NDs in this primary array will now be surrounded by vapor, with low thermal conductivity compared to liquid water, resulting in a temperature increase that promotes further bubble growth (inset in Figure 1b). At the same time, the microbubble so formed will pull in RT water from the surrounding medium, which will cool the secondary array, thereby preventing bubble nucleation there. However, the secondary array will still be hot, resulting in a horizontal temperature gradient on the surface of the microbubble surrounding the primary array. The resulting surface tension gradient will induce directional flow from the warmer to the cooler side of the bubble surface (dark green arrows) and drive the bulk liquid (gray arrows) across the substrate surface in the same direction (as traced by the PS particles). If the laser is instead focused on the gap between the arrays (middle panel), then the bubble will cover both arrays, with its center at the midpoint of the gap. Due to the symmetric heating on the sides of the bubble, only a vertical temperature gradient will appear on the bubble surface, resulting in flow vortices with lateral components toward the bubble on the substrate surface, as observed experimentally.

To substantiate the interpretation above, we show in Figure 2c combined thermal and flow FEM simulations in a plane 0.5 μm above the interface. The simulations utilized the single ND absorption cross sections shown in Figure 1b and a Gaussian intensity profile with the same width as in the experiment. We modeled the bubble as a 0.87 μm radius half-sphere filled with vapor and then self-consistently calculated the temperature distribution, the surface tension gradient over the bubble interface, and the resulting Marangoni flow. For the case of illumination centered on the left and right arrays, good agreement with the experiments was obtained by slightly shifting the center of the bubble by 0.45 μm from the array centers along the connecting symmetry axis and in the direction of the flow. The inset in the left panel compares the calculated flow speed in this case and the speed of the PS beads, estimated from motion blur during the 0.5 ms exposure time of the camera (Figure S7).

Directional Flow Control Based on Asymmetric Array Pairs. Although directional flow control based on tiny shifts in the laser focus position is a fascinating effect, it may be impractical for many applications. However, in a previous study,[60] we demonstrated that similar directional flows could also be achieved by breaking the thermal symmetry of the heating structure using a pair of dissimilar Au ND arrays exposed to a broad laser focus. In Figure 3, we show that this approach also works well for the a-Si ND system. Here, microbubbles nucleate on a primary array of 37 NDs that are separated by a gap of d = 400 nm from the same type of array as that in Figure 2,

https://doi.org/10.1021/acs.jpcc.4c08101
J. Phys. Chem. C 2025, 129, 5502−5510

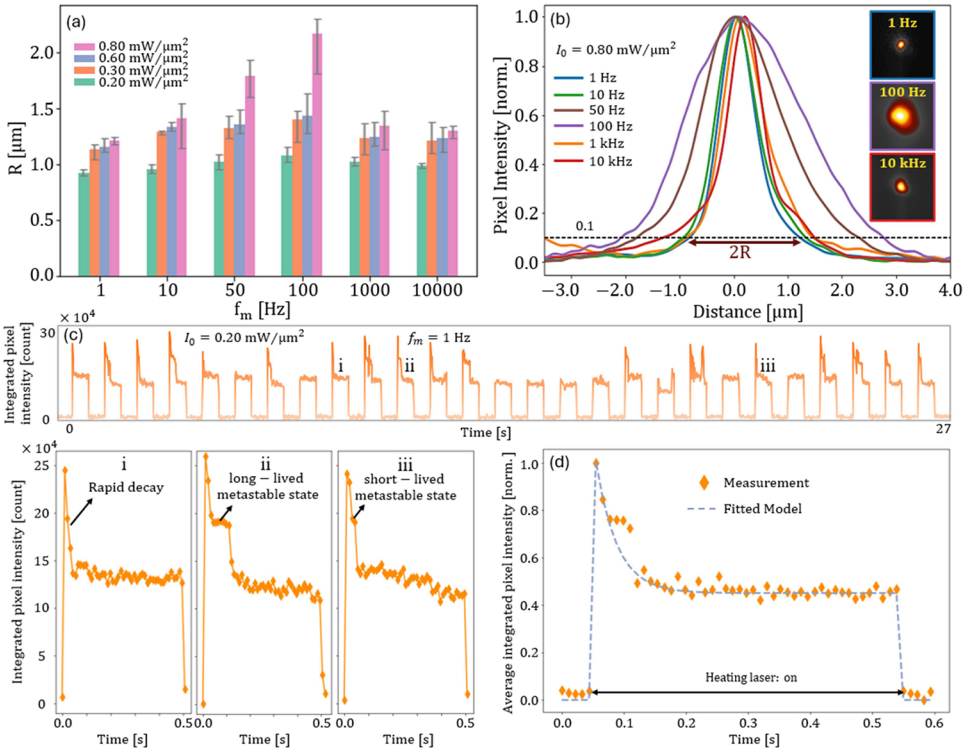

Figure 4. Frequency-dependent bubble dynamics. (a) Apparent bubble radius versus modulation frequency and peak intensity $R(f_m, I_0)$. The error bars indicate variation between three separate ND arrays. (b) Insets show time-averaged dark-field images of microbubbles induced on a 37 ND array for the highest incident laser intensity $I_0 = 0.8$ mW/μm^2 and modulation frequencies $f_m = 1$ Hz, 100 Hz, and 10 kHz. Main graph shows corresponding normalized linecuts through the bubble profile centers for varying f_m. The bubble radius R is defined from the half-width at 10% of peak height as indicated. (c) Integrated dark-field scattering intensity versus time for a bubble induced using $f_m = 1$ Hz and $I_0 = 0.2$ mW/μm^2, with magnifications of three example periods shown in the lower left panels. (d) Sum of all periods shown in (c) together with a fit to constant plus an exponential decay with decay-time = 35 ms. Images were recorded using a camera exposure time of 0.5 ms and frame rate of 75 Hz in (a, b) and 90 Hz in (c).

containing 19 NDs. Since the primary array now will produce about twice the amount of heat as the secondary array, this system is robust against small variations in laser position.

The potential for controlled directional transport of small particles using the asymmetric ND arrays is indicated by the experiment shown in Figure 3a, which was based on first placing a bead on the substrate some distance away from the ND arrays, using optical tweezers, and then recording its trajectory after the heating laser was turned on.[60] In the example shown, we used a 2 μm PS bead and a starting position $r_s = 23$ μm from the primary array in the direction of the expected maximum outward lateral flow. Using the same illumination conditions as shown in Figure 2, the bead displaces $\Delta r = 65$ μm in an almost straight path along the axis connecting the array centers, during the 3 s. observation time, until it moves out of the camera's field of view. As a further illustration, we show in Figure 3b (Video S4) overlaid images of 1 μm diameter PS bead trajectories analogous to those shown in Figure 2a. By utilizing the motion blur, we estimated the lateral particle speeds to ~5 mm/s at a distance of ~5 μm from the primary array, the closest distance that produced clearly discernible tracks, decreasing to ~2.5 mm/s at ~7 μm distance. Due to the increased heating power of the 37 ND array, these speeds are ~1.6 times higher than shown in the inset of Figure 2c, recorded at similar distances from the primary heating array, and in good agreement with the corresponding flow simulation for the asymmetric array pair shown in Figure 3c.

Variation in Particle Displacement with Laser Modulation Frequency. The experiment illustrated in Figure 3a is well suited for investigating the influence of the laser modulation frequency f_m on particle displacement. In Figure 3d, we have plotted the displacement of 2 μm beads observed over $\Delta t = 1.8$ s. against f_m, spanning four decades, for three nominally identical asymmetric ND arrays based on using the same starting position and irradiance as in Figure 3a. The effect of varying f_m is obvious: an increase in the average Δr by ~400%, from ~9 to ~45 μm, for $f_m = 1 \rightarrow 100$ Hz, followed by a decrease to ~33 μm at the highest frequencies. The overall behavior is very similar to what we have previously reported for gold ND arrays,[60] for which particle displacement also exhibited a continuous increase up to $f_m \approx 100$ Hz, followed by saturation and then decrease at higher frequencies. The variation up to $f_m = 100$ Hz could be modeled by assuming that the bead displacement during an illumination cycle ($t = 0 \rightarrow 1/2f_m$) resulted from two components contributing to the particle speed, $u(t, r) = [u_t \exp(-t/\tau) + u_p](r_0/r)^{-3}$, where the exponentially decaying part, with amplitude u_t and decay time τ, represents the strong transient flow associated with nucleation of a bubble, u_p represents the amplitude of the following equilibrium Marangoni flow, and the speed falls off with distance from the microbubble as r^{-3} with characteristic length r_0. However, since the model predicts a continuous increase in displacement with $f_m$while the data exhibit a peak at $f_m = 100$ Hz, it is not possible to find a good fit to the full data set using a constant ratio u_t/u_p. Thus, excluding the 100 Hz data points yields the best fit for $\tau \approx 15$ ms and $u_t/u_p \approx 16$, while excluding the two highest frequencies yields a very different result, $\tau \approx 0.4$ ms and $u_t/u_p \approx 600$. In a previous study,[60] we explained the saturation in displacement for $f_m > 100$ Hz as due to the bubble having no time to fully dissipate during

https://doi.org/10.1021/acs.jpcc.4c08101
J. Phys. Chem. C 2025, 129, 5502−5510

the "dark" intervals between the illumination sequences, resulting in the disappearance of the transient flow component, in agreement with measurements of bubble dissipation times for Au ND arrays of similar sizes by Jones et al.[58] However, even by disregarding the high-frequency points (full line in Figure 3c), the model deviates significantly from the measured data. This indicates that the absolute flow magnitudes also vary with f_m, despite the light intensity and total optical power being constant over an illumination cycle and thus independent of f_m. To obtain some insight into this variation, we now turn to imaging of the photoinduced bubbles.

Variation in Bubble-Size with Laser Modulation Frequency. We investigated the variation in bubble size using single isolated arrays consisting of 37 NDs while keeping the same laser beamwidth as before. Darkfield scattering images of bubble dynamics could be recorded at a framerate of 75 Hz and a camera exposure time of 0.5 ms by zooming in on a small region centered on an ND array. Since the framerate is too low to record dynamics during individual illumination periods for all but the lowest modulation frequencies (see below), we first focus on averages obtained by summing up to 3000 individual frames (total duration ∼40 s). A bubble then produces a close to Gaussian darkfield intensity distribution, from which we define an apparent average bubble radius $\overline{R}$ from the points at which the scattering intensity has dropped to 10% of its maximum value. We note that due to the small size of the bubbles and the limited optical resolution, we cannot determine the three-dimensional shape of the bubbles from these images.

Figure 4a summarizes the variation in $\overline{R}$ with f_m and I_0. The data show an overall similarity to the results displayed in Figure 3d, that is, both the bubble-induced particle displacement and the average bubble size first increase with modulation frequency and then fall off from a maximum at around f_m = 100 Hz. This trend is most pronounced at the highest applied power, I_0 = 0.8 mW/μm^2, as illustrated in Figure 4b. However, for this case, we also observe large fluctuations in bubble appearance during the measurement, which complicates interpretation (Video S5). We next attempted to record the variation in bubble size with time during individual laser heating periods for the lowest modulation frequency, f_m = 1 Hz, using the maximum frame rate available, 90 Hz. Because of the low number of counts per pixel, it turned out to be difficult to directly quantify $R(t)$ with reasonable precision. However, as shown in Figure 4c (Video S6), the integrated darkfield intensity plotted versus time resolves the bubble dynamics, with the caveat that very fast and rare events are unlikely to be captured because of the short integration time and finite length of the image sequence. Each bright state typically begins at a high intensity and then decreases toward a more stable state that is about half as bright. However, in some periods, the initial intensity burst is missing, and in some, it reappears at a later stage. Moreover, the decay from the initial state often occurs in two steps via an intermediate metastable state of varying duration, as highlighted in the three lower left magnifications in Figure 4c. The stepwise decay is also visible in a sum of all periods, Figure 4d, as well as in data collected for the highest laser intensity, I_0 = 0.8 mW/μm^2 (Figure S8).

As mentioned in the introduction, previous investigations of photothermally generated bubbles in air-equilibrated water have revealed complex growth dynamics, beginning with explosive boiling followed by oscillations and exhalation of tiny bubbles, and, finally, a slow diffusion-driven growth phase,[22,50,51,55] which in our case is limited by the size of the isolated ND arrays.[58] The duration of the first phase, in which a large bubble nucleates, expands, and then shrinks, has been estimated to be ∼0.25 ms, while the oscillating bubble phase lasts around 10 ms.[22,51] Based on these earlier reports and the results in Figure 4d, we interpret the increase in $\overline{R}$ from f_m = 1 to 100 Hz seen in Figure 4a as mainly resulting from the increasing weight of these short-time (large R) contributions to the average due to truncation of the long-lived (small R) stable phase. In other words, as the heating duration becomes shorter than the decay time of the initial burst, the stable phase is never reached, leading to an increase in the average bubble size. By further increasing f_m beyond 100 Hz, we expect that bubbles formed during successive heating cycles begin to overlap due to the finite bubble lifetime, resulting in the gradual disappearance of the large R nucleation and oscillation phases. Therefore, only a stable bubble remains on the array, corresponding to the plateau observed in Figure 4c. Hence, $\overline{R}$ at very low modulation frequencies (where the bubble has sufficient time to reach a steady state and remain there until the end of the cycle) and very high modulation frequencies (where the bubble does not have enough time to dissipate, resulting in the loss of the large R transients) would tend to the same value. In this picture, the stepwise intensity decays seen in Figure 4c are likely caused by abrupt bubble volume changes caused by the ejection and occasional reabsorption of microbubbles during the last part of the oscillating phase, when the bubble is close to dynamic equilibrium with its surroundings.

To further investigate the correlation between $\overline{R}(f_m)$ and particle displacement $\Delta r(f_m)$ in Figures 4a and 3d, we performed flow simulations similar to those in Figure 2c for the asymmetric array pair. For a fixed irradiance and at thermal equilibrium, the simulation results (Figure S9) show an increase in directional lateral flow speed u by a factor ∼10 for a change in bubble radius from 0.5 to 1.2 μm. Considering that the Marangoni force F_M, induced by a bubble and acting on the surrounding fluid, is proportional to $\frac{\partial T}{\partial x}R^2$, where $\frac{\partial T}{\partial x}$ is the thermal gradient,[22] this result can be interpreted as the combined effect of the changing bubble size and the evolving thermal gradient across the hemispherical bubble surface as the radius increases. The simulation results can thus qualitatively explain the observed variation in $\Delta r(f_m)$ in terms of a positive correlation between lateral flow speed $u(t)$ and bubble radius $R(t)$ during the modulation frequency-dependent illumination cycle. However, the magnitude of the effect seems far too small to explain the large increase in particle displacement, by ∼400% between f_m = 1 to 100 Hz, seen in Figure 3d. The discrepancy could be due to the assumption of thermal equilibrium in the simulations, which thus neglect flow dynamics associated with bubble nucleation, or it might indicate mechanical resonance effects associated with the periodic injection of photothermal energy into the system. Unfortunately, such time-dependent dynamic effects are beyond the reach of our current simulation capability.

SUMMARY AND OUTLOOK

In this study, we demonstrated the potential of amorphous silicon (a-Si) nanodisks as efficient photothermal heaters for local water vaporization and microbubble generation using time-modulated CW laser illumination. These microbubbles produce strong Marangoni flows capable of displacing microparticles over 40 μm in less than a second, double the distance achieved with gold nanostructures, while operating at significantly lower power densities than most previously reported systems. Finite element method (FEM) simulations revealed that a-Si nano-

https://doi.org/10.1021/acs.jpcc.4c08101
J. Phys. Chem. C 2025, 129, 5502−5510

disks generate higher localized temperatures compared to gold nanostructures, but the heat remains confined, limiting diffusion-driven bubble growth and enabling ultrafast bubble modulation. We also demonstrated that the direction of Marangoni flows can be dynamically controlled by adjusting the heating laser's position or by introducing asymmetry in the nanostructure arrays. Furthermore, we showed that the modulation frequency of the laser influences both the average size of the nucleated vapor bubbles and the total displacement of free particles, highlighting the intricate relationship among thermal gradients, laser power density, and bubble dynamics.

Our findings establish a-Si nanodisks as a promising platform for precise thermal and flow control in microfluidic systems. Their localized heating capabilities make them highly suited to studying microscale boiling and heat transfer processes. Future work could leverage Raman thermometry to capture detailed temperature distributions around the nanodisks, possibly providing new insights into heat transfer dynamics during bubble formation and growth. Further, our results underline the need for more advanced simulation methodologies able to tackle nonequilibrium transient thermal and fluid phenomena, including the bubble nucleation process. Future investigations could also be directed toward alternative nanostructure designs optimized for specific applications, such as targeted drug delivery or chemical mixing. We hope that this study will provide a foundation for further research and applications in those directions.

■ ASSOCIATED CONTENT

Supporting Information

The Supporting Information is available free of charge at https://pubs.acs.org/doi/10.1021/acs.jpcc.4c08101.

Supprting Information: Samples and fabrication, finite element flow simulations, complementary experimental data (PDF)

Video S1: Video graph of 1 μm PS beads driven across the substrate surface near a pair of symmetric heating arrays, when the laser focal point of the time-modulated Gaussian laser beam is positioned on the left array; video plays at 21 fps, which is 1/3 of the original recording frame rate (AVI)

Video S2: As Video S1, but the laser beam is positioned in between the arrays (AVI)

Video S3: As Video S1, but the laser beam is positioned on the right array (AVI)

Video S4: Video graph of 1 μm PS beads driven across the substrate surface near a pair of asymmetric heating arrays; video plays at 21 fps, which is 1/3 of the original recording frame rate (AVI)

Video S5: Fluctuations in bubble appearance at a modulation frequency of f_m = 100 Hz and an intensity of I_0 = 0.8 mW/μm^2; video plays at 13 fps, which is 1/5 of the original recording frame rate (AVI)

Video S6: Bubble dynamics during a single heating cycle at a modulation frequency of f_m = 1 Hz and an intensity of I_0 = 0.2 mW/μm^2; video plays at 9 fps, which is 1/10 of the original recording frame rate (MP4)

■ AUTHOR INFORMATION

Corresponding Authors

Pantea Dara − *Department of Physics, Chalmers University of Technology, 41296 Gothenburg, Sweden;* orcid.org/0000-0002-4536-193X; Email: pantea.dara@chalmers.se

Mikael Käll − *Department of Physics, Chalmers University of Technology, 41296 Gothenburg, Sweden;* orcid.org/0000-0002-1163-0345; Email: mikael.kall@chalmers.se

Complete contact information is available at: https://pubs.acs.org/10.1021/acs.jpcc.4c08101

Author Contributions

The manuscript was written through contributions of all authors. All authors have given approval to the final version of the manuscript.

Notes

The authors declare no competing financial interest.

■ ACKNOWLEDGMENTS

This work was supported by the Swedish Research Council (contract no. 2020-04063). We gratefully acknowledge Mahdi Shanei for providing the nanostructured a-Si samples, which were fabricated at Myfab Chalmers.

■ REFERENCES

(1) Baffou, G. *Thermoplasmonics: Heating Metal Nanoparticles Using Light*; Cambridge University Press: Cambridge, 2017.

(2) Zheng, Y.; Liu, H.; Wang, Y.; Zhu, C.; Wang, S.; Cao, J.; Zhu, S. Accumulating microparticles and direct-writing micropatterns using a continuous-wave laser-induced vapor bubble. *Lab Chip* **2011**, *11* (22), 3816−3820.

(3) Bangalore Rajeeva, B.; Lin, L.; Perillo, E. P.; Peng, X.; Yu, W. W.; Dunn, A. K.; Zheng. High-Resolution Bubble Printing of Quantum Dots. *ACS Appl. Mater. Interfaces* **2017**, *9* (19), 16725−16733.

(4) Jones, S.; Andren, D.; Karpinski, P.; Kall, M. Photothermal Heating of Plasmonic Nanoantennas: Influence on Trapped Particle Dynamics and Colloid Distribution. *ACS Photonics* **2018**, *5* (7), 2878−2887.

(5) Karim, F.; Vasquez, E. S.; Sun, Y.; Zhao, C. Optothermal microbubble assisted manufacturing of nanogap-rich structures for active chemical sensing. *Nanoscale* **2019**, *11* (43), 20589−20597.

(6) Kim, Y.; Ding, H.; Zheng, Y. Enhancing surface capture and sensing of proteins with low-power optothermal bubbles in a biphasic liquid. *Nano Lett.* **2020**, *20* (10), 7020−7027.

(7) Ciraulo, B.; Garcia-Guirado, J.; de Miguel, I.; Ortega Arroyo, J.; Quidant, R. Long-range optofluidic control with plasmon heating. *Nat. Commun.* **2021**, *12* (1), 2001.

(8) Karim, F.; Sun, Y.; Vasquez, E. S.; Zhao, C. *Active and Ultrasensitive Chemical and Biosensing through Optothermally Generated Microbubble. in Conference on Lasers and Electro-Optics*; Optica Publishing Group: Washington, DC, 2020.

(9) Chen, J.; Zeng, Y.; Zhou, J.; Wang, X.; Jia, B.; Miyan, R.; Zhang, T.; Sang, W.; Wang, Y.; Qiu, H.; Qu, J. Optothermophoretic flipping method for biomolecule interaction enhancement. *Biosens. Bioelectron.* **2022**, *204*, No. 114084.

(10) Hu, M.; Petrova, H.; Hartland, G. V. Investigation of the properties of gold nanoparticles in aqueous solution at extremely high lattice temperatures. *Chemical physics letters* **2004**, *391* (4−6), 220−225.

(11) Plech, A.; Kotaidis, V.; Grésillon, S.; Dahmen, C.; Von Plessen, G. Laser-induced heating and melting of gold nanoparticles studied by time-resolved x-ray scattering. *Phys. Rev. B* **2004**, *70* (19), No. 195423.

(12) Carlson, M. T.; Green, A. J.; Richardson, H. H. Superheating water by CW excitation of gold nanodots. *Nano Lett.* **2012**, *12* (3), 1534−1537.

(13) Hühn, D.; Govorov, A.; Gil, P. R.; Parak, W. J. Photostimulated Au nanoheaters in polymer and biological media: characterization of mechanical destruction and boiling. *Adv. Funct. Mater.* **2012**, *22* (2), 294−303.
(14) Fang, Z.; Zhen, Y. R.; Neumann, O.; Polman, A.; García de Abajo, F. J.; Nordlander, P.; Halas, N. J. Evolution of light-induced vapor generation at a liquid-immersed metallic nanoparticle. *Nano Lett.* **2013**, *13* (4), 1736−1742.
(15) Namura, K.; Nakajima, K.; Kimura, K.; Suzuki, M. Photothermally controlled Marangoni flow around a micro bubble. *Appl. Phys. Lett.* **2015**, *106* (4), No. 043101.
(16) Namura, K.; Nakajima, K.; Kimura, K.; Suzuki, M. Microfluidic control on nanoplasmonic thin films using Marangoni effect. *J. Nanophotonics* **2016**, *10* (3), No. 033006.
(17) Namura, K.; Nakajima, K.; Kimura, K.; Suzuki, M. Sheathless particle focusing in a microfluidic chamber by using the thermoplasmonic Marangoni effect. *Appl. Phys. Lett.* **2016**, *108* (7), No. 071603.
(18) Namura, K.; Nakajima, K.; Suzuki, M. Quasi-stokeslet induced by thermoplasmonic Marangoni effect around a water vapor microbubble. *Sci. Rep.* **2017**, *7* (1), 45776.
(19) Namura, K.; Nakajima, K.; Suzuki, M. Investigation of transition from thermal- to solutal-Marangoni flow in dilute alcohol/water mixtures using nano-plasmonic heaters. *Nanotechnology* **2018**, *29* (6), No. 065201.
(20) Namura, K.; Okai, S.; Kumar, S.; Nakajima, K.; Suzuki, M. Self-Oscillation of Locally Heated Water Vapor Microbubbles in Degassed Water. *Adv. Mater. Interfaces* **2020**, *7* (18), No. 2000483.
(21) Hiroshige, N.; Okai, S.; Zhang, X.; Kumar, S.; Namura, K.; Suzuki, M. Microbubble oscillation on localized heat source affected by dissolved gases in water. *J. Appl. Phys.* **2024**, *135* (9), No. 094701.
(22) Namura, K.; Iwasaki, T.; Nakajima, K.; Suzuki, M. Round-trip motion of air-rich bubbles exhaled from a vapor-rich bubble generated at a local heating point. *J. Appl. Phys.* **2024**, *135* (21), 214702.
(23) Setoura, K.; Ito, S.; Miyasaka, H. Stationary bubble formation and Marangoni convection induced by CW laser heating of a single gold nanoparticle. *Nanoscale* **2017**, *9* (2), 719−730.
(24) Liu, X.; Bao, L.; Dipalo, M.; De Angelis, F.; Zhang, X. Formation and dissolution of microbubbles on highly-ordered plasmonic nanopillar arrays. *Sci. Rep.* **2015**, *5* (1), 18515.
(25) Baffou, G.; Polleux, J.; Rigneault, H.; Monneret, S. Super-heating and micro-bubble generation around plasmonic nanoparticles under cw illumination. *J. Phys. Chem. C* **2014**, *118* (9), 4890−4898.
(26) Andrén, D.; Baranov, D. G.; Jones, S.; Volpe, G.; Verre, R.; Käll, M. Microscopic metavehicles powered and steered by embedded optical metasurfaces. *Nat. Nanotechnol.* **2021**, *16* (9), 970−974.
(27) Dong, Y.; Xu, Z.; Li, N.; Tong, J.; Fu, Y. H.; Zhou, Y.; Hu, T.; Zhong, Q.; Bliznetsov, V.; Zhu, S.; Lin, Q. Si metasurface half-wave plates demonstrated on a 12-in. CMOS platform. *Nanophotonics* **2020**, *9* (1), 149−157.
(28) Khorasaninejad, M.; Chen, W. T.; Devlin, R. C.; Oh, J.; Zhu, A. Y.; Capasso, F. Metalenses at visible wavelengths: Diffraction-limited focusing and subwavelength resolution imaging. *Science* **2016**, *352* (6290), 1190−1194.
(29) Khorasaninejad, M.; Zhu, A. Y.; Roques-Carmes, C.; Chen, W. T.; Oh, J.; Mishra, I.; Devlin, R. C.; Capasso, F. Polarization-insensitive metalenses at visible wavelengths. *Nano Lett.* **2016**, *16* (11), 7229−7234.
(30) Staude, I.; Schilling, J. Metamaterial-inspired silicon nanophotonics. *Nat. Photonics* **2017**, *11* (5), 274−284.
(31) Khorasaninejad, M.; Crozier, K. B. Silicon nanofin grating as a miniature chirality-distinguishing beam-splitter. *Nat. Commun.* **2014**, *5* (1), 5386.
(32) Zograf, G. P.; Petrov, M. I.; Zuev, D. A.; Dmitriev, P. A.; Milichko, V. A.; Makarov, S. V.; Belov, P. A. Resonant nonplasmonic nanoparticles for efficient temperature-feedback optical heating. *Nano Lett.* **2017**, *17* (5), 2945−2952.
(33) Danesi, S.; Gandolfi, M.; Carletti, L.; Bontempi, N.; De Angelis, C.; Banfi, F.; Alessandri, I. Photo-induced heat generation in non-plasmonic nanoantennas. *Phys. Chem. Chem. Phys.* **2018**, *20* (22), 15307−15315.
(34) Tian, J.; Luo, H.; Li, Q.; Pei, X.; Du, K.; Qiu, M. Near-infrared super-absorbing all-dielectric metasurface based on single-layer germanium nanostructures. *Laser Photonics Rev.* **2018**, *12* (9), No. 1800076.
(35) Li, Y.; Yang, X.; Yang, Y.; Wang, B.; Li, X.; Salas-Montiel, R. Optical nanoheating of resonant silicon nanoparticles. *Opt. Express* **2019**, *27* (21), 30971−30978.
(36) Duh, Y. S.; Nagasaki, Y.; Tang, Y. L.; Wu, P. H.; Cheng, H. Y.; Yen, T. H.; Ding, H. X.; Nishida, K.; Hotta, I.; Yang, J. H.; Lo, Y. P. Giant photothermal nonlinearity in a single silicon nanostructure. *Nat. Commun.* **2020**, *11* (1), 4101.
(37) Tsoulos, T. V.; Tagliabue, G. Self-induced thermo-optical effects in silicon and germanium dielectric nanoresonators. *Nanophotonics* **2020**, *9* (12), 3849−3861.
(38) Assadillayev, A.; Hinamoto, T.; Fujii, M.; Sugimoto, H.; Raza, S. Thermal near-field tuning of silicon Mie nanoparticles. *Nanophotonics* **2021**, *10* (16), 4161−4169.
(39) Li, C. H.; Tang, Y. L.; Takahara, J.; Chu, S. W. Nonlinear heating and scattering in a single crystalline silicon nanostructure. *J. Chem. Phys.* **2021**, *155* (20), 204202.
(40) Zograf, G. P.; Petrov, M. I.; Makarov, S. V.; Kivshar, Y. S. All-dielectric thermonanophotonics. *Advances in Optics and Photonics* **2021**, *13* (3), 643−702.
(41) González-Colsa, J.; Olarte-Plata, J. D.; Bresme, F.; Albella, P. Enhanced thermo-optical response by means of anapole excitation. *J. Phys. Chem. Lett.* **2022**, *13* (26), 6230−6235.
(42) Ishii, S.; Tanjaya, N. K.; Shkondin, E.; Murai, S.; Takayama, O. Optical absorption and heat conduction control in high aspect ratio silicon nanostructures for photothermal heating applications. *Applied Materials Today* **2023**, *32*, No. 101824.
(43) Milichko, V. A.; Zuev, D. A.; Baranov, D. G.; Zograf, G. P.; Volodina, K.; Krasilin, A. A.; Mukhin, I. S.; Dmitriev, P. A.; Vinogradov, V. V.; Makarov, S. V.; Belov, P. A. Metal-dielectric nanocavity for real-time tracing molecular events with temperature feedback. *Laser Photonics Rev.* **2018**, *12* (1), No. 1700227.
(44) Zograf, G. P.; Timin, A. S.; Muslimov, A. R.; Shishkin, I. I.; Nominé, A.; Ghanbaja, J.; Ghosh, P.; Li, Q.; Zyuzin, M. V.; Makarov, S. V. All-optical nanoscale heating and thermometry with resonant dielectric nanoparticles for controllable drug release in living cells. *Laser Photonics Rev.* **2020**, *14* (3), No. 1900082.
(45) Archetti, A.; Lin, R. J.; Restori, N.; Kiani, F.; Tsoulos, T. V.; Tagliabue, G. Thermally reconfigurable metalens. *Nanophotonics* **2022**, *11* (17), 3969−3980.
(46) Hong, I.; Anyika, T.; Hong, C.; Yang, S.; Ndukaife, J. C. Hybrid Optical and Diffusiophoretic Nanomanipulation Using All-Dielectric Anapole-Enhanced Thermonanophotonics. *ACS Photonics* **2023**, *10* (11), 4038−4044.
(47) Yang, S.; Ndukaife, J.C. Optofluidic transport and assembly of nanoparticles using an all-dielectric quasi-BIC metasurface. *Light: Sci. Appl.* **2023**, *12* (1), 188.
(48) Zapka, W.; Ziemlich, W.; Tam, A. C. Efficient pulsed laser removal of 0.2 μm sized particles from a solid surface. *Applied physics letters* **1991**, *58* (20), 2217−2219.
(49) Tam, A. C.; Leung, W. P.; Zapka, W.; Ziemlich, W. Laser-cleaning techniques for removal of surface particulates. *J. Appl. Phys.* **1992**, *71* (7), 3515−3523.
(50) Wang, Y.; Zaytsev, M. E.; The, H. L.; Eijkel, J. C.; Zandvliet, H. J.; Zhang, X.; Lohse, D. Vapor and gas-bubble growth dynamics around laser-irradiated, water-immersed plasmonic nanoparticles. *ACS Nano* **2017**, *11* (2), 2045−2051.
(51) Wang, Y.; Zaytsev, M. E.; Lajoinie, G.; The, H. L.; Eijkel, J. C.; van den Berg, A.; Versluis, M.; Weckhuysen, B. M.; Zhang, X.; Zandvliet, H. J.; Lohse, D. Giant and explosive plasmonic bubbles by delayed nucleation. *Proc. Natl. Acad. Sci. U. S. A.* **2018**, *115* (30), 7676−7681.
(52) Li, X.; Wang, Y.; Zaytsev, M. E.; Lajoinie, G.; Le The, H.; Bomer, J. G.; Eijkel, J. C.; Zandvliet, H. J.; Zhang, X.; Lohse, D. Plasmonic

https://doi.org/10.1021/acs.jpcc.4c08101
J. Phys. Chem. C 2025, 129, 5502−5510

bubble nucleation and growth in water: Effect of dissolved air. *J. Phys. Chem. C* **2019**, *123* (38), 23586−23593.
(53) Zaytsev, M. E.; Wang, Y.; Zhang, Y.; Lajoinie, G.; Zhang, X.; Prosperetti, A.; Zandvliet, H. J.; Lohse, D. Gas−vapor interplay in plasmonic bubble shrinkage. *J. Phys. Chem. C* **2020**, *124* (10), 5861−5869.
(54) Hou, L.; Yorulmaz, M.; Verhart, N. R.; Orrit, M. Explosive formation and dynamics of vapor nanobubbles around a continuously heated gold nanosphere. *New J. Phys.* **2015**, *17* (1), No. 013050.
(55) Li, F.; Gonzalez-Avila, S. R.; Nguyen, D. M.; Ohl, C. D. Oscillate boiling from microheaters. *Physical Review Fluids* **2017**, *2* (1), No. 014007.
(56) Namura, K.; Imafuku, S.; Kumar, S.; Nakajima, K.; Sakakura, M.; Suzuki, M. Direction control of quasi-stokeslet induced by thermoplasmonic heating of a water vapor microbubble. *Sci. Rep.* **2019**, *9* (1), 4770.
(57) Namura, K.; Hanai, S.; Kondo, S.; Kumar, S.; Suzuki, M. Gold Micropetals Self-Assembled by Shadow-Sphere Lithography for Optofluidic Control. *Adv. Mater. Interfaces* **2022**, *9* (18), No. 2200200.
(58) Jones, S.; Andrén, D.; Antosiewicz, T. J.; Kall, M. Ultrafast Modulation of Thermoplasmonic Nanobubbles in Water. *Nano Lett.* **2019**, *19* (11), 8294−8302.
(59) Jones, S.; Andrén, D.; Antosiewicz, T. J.; Stilgoe, A.; Rubinsztein-Dunlop, H.; Kall, M. Strong Transient Flows Generated by Thermoplasmonic Bubble Nucleation. *ACS Nano* **2020**, *14* (12), 17468−17475.
(60) Dara, P.; Shanei, M.; Jones, S.; Käll, M. Directional control of transient flows generated by thermoplasmonic bubble nucleation. *J. Phys. Chem. C* **2023**, *127* (35), 17454−17459.
(61) Todisco, F.; Malureanu, R.; Wolff, C.; Gonçalves, P. A. D.; Roberts, A. S.; Mortensen, N. A.; Tserkezis, C. Magnetic and electric Mie-exciton polaritons in silicon nanodisks. *Nanophotonics* **2020**, *9* (4), 803−814.

https://doi.org/10.1021/acs.jpcc.4c08101
J. Phys. Chem. C 2025, 129, 5502−5510